Title

Direct visualisation of ligands on gold nanoparticles in a liquid environment

Author list

Adrián Pedrazo-Tardajos[1, 2, ¶], Nathalie Claes[1, 2, ¶], Da Wang [1, 2, ¶], Ana Sánchez-Iglesias[3,4], Proloy Nandi[1,2], Kellie Jenkinson [1, 2], Robin De Meyer [1, 2], Luis M. Liz-Marzán[3,4,5,6] and Sara Bals[1, 2, *]

Affiliations

[1] EMAT-University of Antwerp, Groenenborgerlaan 171, 2020 Antwerp, Belgium

[2] NANOlab Center of Excellence, University of Antwerp, Belgium

[3] CIC biomaGUNE, Paseo de Miramon 182, 20009 Donostia-San Sebastián, Spain

[4] Centro de Investigación Biomédica en Red, Bioingeniería, Biomateriales y Nanomedicina, CIBER-BBN, Paseo de Miramon 182, 20009 Donostia-San Sebastián, Spain

[5] Ikerbasque, Basque Foundation for Science, 48013 Bilbao, Spain

[6] Cinbio, Universidade de Vigo, 36310 Vigo, Spain

¶ These authors contributed equally to this work

*Corresponding author: Sara.Bals@uantwerpen.be

Abstract

The interaction among Au nanoparticles, their surface ligands and the solvent critically influences the properties of nanoparticles. Despite employing spectroscopic and scattering techniques to investigate their ensemble structure, a comprehensive understanding at the nanoscale remains elusive. Electron microscopy enables characterization of the local structure and composition but is limited by insufficient contrast, electron beam sensitivity and ultra-high vacuum, which prevent the investigation of dynamic aspects. Here we show that, by exploiting high-quality graphene liquid cells, we can overcome these limitations and investigate the structure of the ligand shell around the Au nanoparticles, as well as the ligand-Au interface in a liquid environment. Using this graphene liquid cell, we visualize the anisotropy, composition and dynamics of ligand distribution at the Au nanorod surface. Our results indicate a micellar model for the surfactant organisation. This work opens up a reliable and direct visualization of ligand distribution around colloidal nanoparticles.

Main text

Gold nanoparticles have been a topic of intense research for several decades due to their potential applications in various fields[1]. The synthesis of colloidal nanocrystals (NCs) with controllable shapes and sizes can be considered a mature field of research and was recently rewarded by the Nobel Prize in Chemistry[2,3]. It is widely accepted that surface ligands may influence NC growth by preferentially binding on certain crystallographic facets and consequently altering their surface energy[4,5]. For example, cetyltrimethylammonium bromide (CTAB) has become the main surfactant – often called shape-directing agent – in the seed-mediated growth of anisotropic Au NCs. Based on scattering[6–8] and spectroscopy techniques[9–13], a surfactant layer thickness of 32 Å was measured, resulting in a widely reported model of CTAB molecules that form a partially interdigitated bilayer structure[10] at the surface of Au nanorods (NRs). Moreover, it was found that the grafting density of CTAB may vary over the surface of individual Au NRs. However, these characterization techniques correspond to ensemble measurements and thus cannot reveal the *local* structure and distribution of CTAB ligands on a single particle level. On the other hand, molecular dynamics simulations suggested that CTAB may form elongated surfactant micelles on Au NRs, leaving water channels containing bromide ions that provide a path for the diffusion of reactants toward the NR surface[14,15].

Based on these studies, it becomes clear that we do not have yet a complete picture of the way CTAB molecules are organized at the surface of Au NRs and whether their distribution is uniform or heterogeneous. Moreover, it is still unclear whether their organisation is static or dynamic and if surfactant organisation and behaviour is the same for all Au NRs in a colloidal dispersion. One may expect that transmission electron microscopy (TEM), a technique that enables one to investigate nanostructures down to the atomic scale, would be a useful approach to investigate the CTAB shell at the surface of individual Au NRs. Although a handful TEM

studies have been dedicated to investigate in detail the interface between Au NCs and CTAB[16–18], they did not afford direct ligand imaging. The main bottleneck is the relatively low atomic number of the atoms present in CTAB molecules, resulting in insufficient image contrast. This problem is especially challenging when using conventional TEM support grids, which contain a ~20 nm thick carbon layer that dramatically reduces the contrast obtained for surface ligands. A solution to this problem is the use of graphene as an ultrathin TEM support, which minimizes the background signal and thus leads to an improved contrast for the surface ligands, as has been illustrated by Lee *et al.* [19]. Graphene moreover exhibits excellent thermal and electrical conductivity, which makes it possible to notably reduce charging effects and radiation damage during TEM investigation[20–24]. Therefore, graphene supports have been proven to be of great value for TEM characterization of soft-hard interfaces[19,25], organic samples[26], molecules[27], proteins[28], and even ligands[18,19,29].

Graphene grids were recently used in a study by Janicek *et al.* where electron energy loss spectroscopy (EELS) was applied to investigate the CTAB shell around Au NRs[18]. It is important to note that, a major drawback related to spectroscopic TEM techniques is the need for relatively long acquisition times and high electron doses, which may lead to alteration of the structure during acquisition. Even more important is the fact that, despite this great progress, all TEM studies of CTAB ligands were performed under conventional TEM conditions, *i.e.* in high vacuum. Samples are hereby prepared by depositing a drop of the colloidal dispersion on a TEM grid and, therefore, drying forces are expected to alter the distribution and structure of surface ligands, as compared to those in the original liquid environment. Although cryo TEM mitigates structural alteration because of capillary forces and has enabled the visualization of metal-containing ligands[13], the approach is not applicable to directly imaging short ligands composed of low Z atoms (e.g., short carbon-chain based) ligands on small NPs. Moreover, the vitreous ice layer (typical thickness ~100 nm) further

compromises the image contrast. When investigating ligand shells surrounding Au NCs in a dried or cryogenic (and therefore static) state, no insights on the dynamic behaviour of ligands in the colloidal dispersion can be possibly obtained. It is therefore clear that further progress is required if we want to directly visualise the real structure of surface ligands together with their dynamic behaviour.

Here we demonstrate the use of TEM to study ligands on single crystalline (SC) Au NRs inside graphene liquid cells (GLCs). GLCs have been previously applied for observation of NC growth, etching, and self-assembly[30,31]. However, to image low-contrast CTAB ligands in a liquid environment with sufficient contrast, it is crucial that polymer residues which are typically derived from graphene transfer, are completely removed. High quality GLCs were therefore prepared through an improved protocol for graphene transfer. Our results demonstrate that the measured thickness of the CTAB layer crucially depends on the presence and the amount of liquid in the GLC. A similar discrepancy between dried and wet state was observed for Au NRs capped with thiol-terminated polyethylene glycol (PEG-SH), thus confirming the importance of studying NC-adsorbed ligands in a liquid environment. The liquid environment additionally enabled us to gather preliminary information on the dynamics of CTAB micelles in a colloidal Au NR dispersion. We furthermore investigated the distribution of chemical elements near the Au-CTAB interface while in the liquid, which again is only possible when high quality GLCs are employed. Energy dispersive X-ray (EDX) spectroscopy analysis included the investigation of the possible presence of Ag, often claimed to be a shape-directing additive during the growth of SC Au NRs but the precise mechanism still being under debate[32–34]. The unique possibility of directly deciphering the structure, composition, and dynamics of CTAB at the surface of Au NRs is envisaged to shed light on its role during Au NC growth.

Results and discussion

Visualization of ligands: from dried state to liquid environment

Monodisperse SC Au NRs (88 ± 3 nm × 22 ± 1 nm; Supplementary Fig. 1a,b) were prepared *via* a silver-assisted seeded growth method[35], followed by washing and redispersion in CTAB solution (1 mM, corresponding to the critical micelle concentration, CMC). Our earlier work showed that nanorods prepared in this manner yield an octagonal cross section displaying {520} lateral facets capped by {110} and {100} tips[36]. To investigate possible drying effects when visualising ligands at the Au NR surface under conventional TEM conditions, we first drop casted the dispersion on a home-made graphene TEM grid, followed by drying under ambient conditions (Fig. 1a-c)[37]. Graphene is an excellent alternative to conventional TEM grids when imaging surface ligands[18,19]. However, the graphene transfer procedure for grid production involves polymers, typically polymethyl methacrylate (PMMA), which often leave residues on the grids[38]. Such residues may induce polymerization and fixation of hydrocarbon molecules during electron illumination, thereby hampering the direct visualisation of surface ligands. These limitations can be overcome by using cellulose acetate butyrate (CAB), a readily accessible polymer[39], which can be effectively removed by heating the graphene grid embedded in activated carbon, a method that is often used to remove organic residues from the surface of TEM grids[40–42]. Further experimental details are provided in the Methods section and in Supplementary Fig. 2, whereas a demonstration of the superior quality of the graphene grids in comparison to commercially available grids is presented in the Extended Fig. 1 and Supplementary Fig. 3.
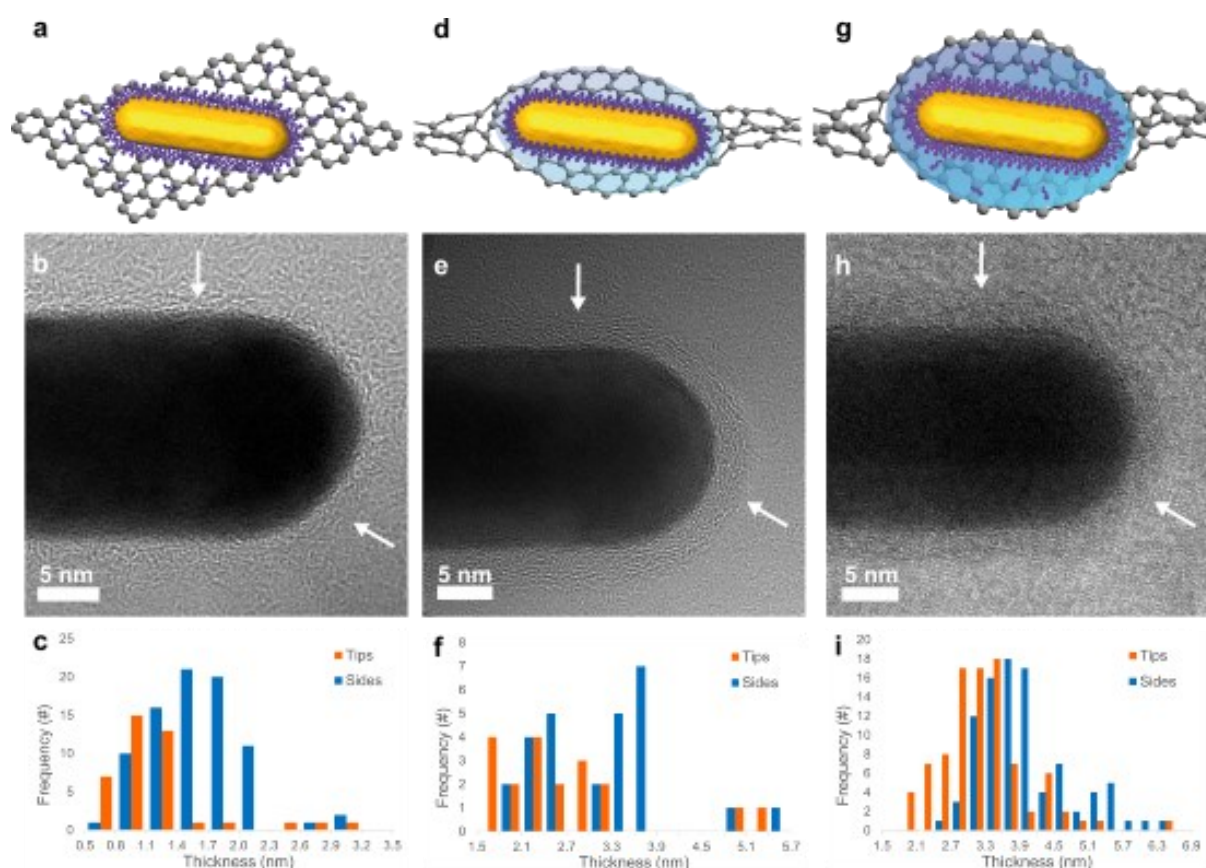
Fig. 1. Comparison of TEM investigation of gold NRs capped with CTAB ligands in dried state on a graphene grid and in a liquid environment. a, Schematic illustration of a gold NR on a graphene grid. b, AC-HRTEM image illustrating the CTAB shell, indicated by white arrows. c, Histogram showing ligand shell thickness at NR tips and lateral sides (average values, 1.21 ± 0.08 nm and 1.37 ± 0.05 nm, respectively). d, Schematic illustration of a GLC with a thin layer of liquid around a gold NR. e, AC-HRTEM image illustrating the CTAB shell, indicated by white arrows. f, Histogram showing the ligand shell thickness at NR tips and lateral sides (average values, 2.61 ± 0.23 nm and 3.02 ± 0.18 nm, respectively). g, Schematic illustration of a GLC with a thick layer of liquid around a gold NR. h, AC-HRTEM image illustrating the CTAB shell, indicated by white arrows. i, Histogram showing the ligand shell thickness at NR tips and lateral sides (average values, 3.22 ± 0.08 nm and 3.71 ± 0.08 nm, respectively).

Aberration-corrected high-resolution transmission electron microscopy (AC-HRTEM) imaging was then performed on CTAB-capped Au NRs, drop cast on home-made graphene grids (Fig. 1b), using an AC-TEM operated at 80 kV with a monochromated electron beam and a negative spherical aberration ($C_s = -5$ μm). Under the negative spherical aberration condition,

the contrast of light elements can be enhanced[43], so that structural features corresponding to ligands[29,44] can be observed, as indicated by white arrows in Fig. 1b. In contrast, ligand visualisation is largely hampered for systems deposited on conventional TEM grids, even when using ultra-thin amorphous carbon supports (Supplementary Fig. 4a-c). These observations demonstrate the importance of using high-quality graphene as the substrate for direct visualisation of surface ligands.

The thickness of the CTAB shell was measured at both the tips and the sides of several Au NRs deposited on graphene grids (Fig. 1c; Supplementary Fig. 5; Supplementary Table 1) and the mean values and corresponding standard errors were found to be 1.21 ± 0.08 nm and 1.37 ± 0.05 nm, respectively. These values are significantly smaller than the CTAB bilayer thickness (3.2-3.4 nm), reported from scattering-based techniques[6,7] and from computer simulations[45]. This discrepancy is likely related to capillary forces inducing collapse of ligands upon drying the colloidal dispersion during TEM sample preparation, which indicates that interpretation of ligand distribution based on TEM measurements in dried state should be carried out with reservation.

Next, we performed graphene encapsulation of the CTAB-stabilized Au NRs dispersion (Fig. 1d-i; Supplementary Fig. 6a-d). Graphene encapsulation results in regions of nanoconfinement and has been successfully implemented in the past to study *in situ* growth of colloidal nanoparticles (NPs)[46,47]. However, to visualise ligands with sufficient contrast in GLCs, it is of great importance that polymer residues derived from graphene transfer are minimized, which is the case when exploiting the approach presented in this work. The GLC[31] was sealed by removing the solution between an ultra-clean graphene grid at the bottom of a petri dish containing the colloidal dispersion and a graphene flake floating on the solution-air interface (Supplementary Fig. 6c,d; See Methods section for more details).

The preparation of the GLCs was validated by Fourier transformations of TEM images, confirming the presence of graphene (Supplementary Fig. 7a,b). We also observed the formation of bubbles and motion of Au NRs, which is additional proof that Au NRs were encapsulated in the GLC (yellow arrows in Supplementary Movie 1). This conclusion is supported by EELS, as presented in Supplementary Fig. 8. These measurements indicate a plasmon peak around 23.2 eV, which have been previously reported for water[48] and the oxygen K-edge inside the GLC. From low loss EELS measurements combined with the log-ratio routine (See Methods section for details), we extracted the thickness of the GLCs and found it to vary between 30 and 95 nm. The average thickness obtained for 10 measured GLCs was approximately 45 nm (Supplementary Table 2). This value is in good agreement with measurements based on TEM and scanning transmission electron microscopy (STEM) images for tilted GLCs (Supplementary Fig. 9). Fig. 1e and h show AC-HRTEM images with lower and higher background contrast, corresponding to GLCs with relatively small and large thickness, respectively. Although Fig. 1h clearly shows the presence of a shell at the Au NR surface, no detailed structure can be appreciated because of the low contrast of ligands in the presence of the surrounding liquid. From the thinner GLC, depicted in Fig. 1e, a more detailed structure for the CTAB shell at the Au NR surface, with thread-like features entangled with each other, can be observed. For both types of GLCs, we measured the thickness of the CTAB layer at different regions on the Au NRs (Fig. 1f and i; Supplementary Figs. 10 and 11; Supplementary Table 1). For the thick GLC, we found that the ligand shell on the tips (3.22 $\pm$ 0.08 nm) was significantly thinner than that on the lateral facets (3.71 $\pm$ 0.08 nm). These values are in good agreement with the reported thickness of CTAB layers based on (averaged) ensemble measurements in liquid and with molecular dynamics simulations[6,7,45]. For the GLC with less liquid, we measured a CTAB shell thickness of 2.61 $\pm$ 0.23 nm at the tips and 3.02 $\pm$ 0.18 nm at the lateral facets, which is significantly smaller compared to the values measured in

GLCs with a thicker layer of liquid. This indicates that the CTAB shell for the thin GLC is likely partially hydrated and, even though a more detailed structure can be appreciated, the interpretation of this apparently layered structure should be made with reservation. Our results demonstrate that relevant measurements of the ligand shell thickness require the presence of a sufficient amount of liquid. This conclusion does not only apply to CTAB, but also when comparing PEG-SH capped Au NRs in wet and dried state (see Supplementary information for sample preparation details; Extended Figs. 2 and 3), a similar trend was observed. Although it is not straightforward to quantify the optimum thickness of the GLC, we estimate that a thickness of 45 nm would be sufficient for Au NRs encapsulated by CTAB, based on the statistics presented in Supplementary Table 2, in correlation with the observation of bubbles forming within such GLCs.

Organization of the ligand shell

Because of the need for a sufficiently thick liquid background, direct visualisation of the internal structure of the CTAB shell remains non-trivial, also because images such as those in Figure 1 correspond to a 2D projection of the CTAB configuration on a cylindrical-shaped Au NR. On the other hand, our local measurements (Fig. 1i), indicate that the shell thickness is not uniform, being affected by curvature and/or the nature of surface facets[18]. Moreover, it is interesting to note that the CTAB organization at the Au NR surface shows notable variability for different NRs. Fig. 2 directly shows examples of the variability of the CTAB, illustrated by a NR for which the CTAB layer is much less apparent at the tip (Fig. 2a), a NR with shell thickness varying along the surface (Fig. 2b), and a NR with a patchy shell (Fig. 2c).
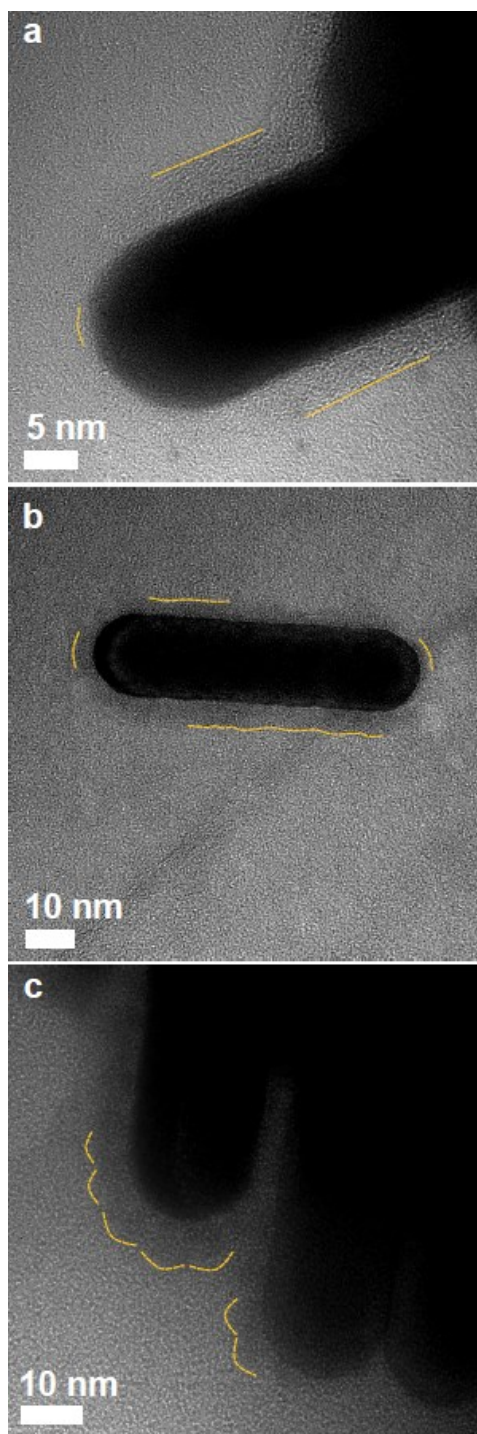
Fig. 2. AC-HRTEM images of different gold NRs capped with CTAB ligands in a liquid environment. a, NR for which the CTAB shell is much less apparent at the tip. b, NR with a varying CTAB shell thickness. c, NR with a patchy CTABshell. Yellow dashed lines are drawn to facilitate observation of the ligand shells. The corresponding images without dashed lines are shown in Supplementary Fig. 12.

.

The variability of the CTAB shell was also discussed by Janicek *et al.*[18], based on EELS measurements performed in dried state. On the other hand, drying effects may have been responsible for the observed deviations from a uniform shell in that case. Since not only drying effects, but also electron beam effects should be avoided, the applied electron dose in this study was always kept below 500 e$^-$/Å^2 during TEM imaging, within the range that is commonly used to visualise organic structures in liquid[49] (See Methods section for details). A dedicated validation experiment was additionally performed, in which AC-HRTEM images recorded before and after 3 minutes of beam exposure were compared (Supplementary Fig. 13) and no critical changes in shell thickness and organization were observed. These observations are in good agreement with previous reports on the scavenger effect provided by graphene during liquid TEM experiments of radiation-sensitive materials[50,51]. Moreover, although the pressure inside a GLC can be as high as 400 MPa[52,53], ligand deformation is not expected at this pressure.

Although a CTAB bilayer could be expected to result in a uniform layer with homogenous thickness, the observations in Fig. 2 support a model in which CTAB micelles are present at the Au surface and not necessarily connected to each other. It is worth mentioning that Meena and Sulpizi demonstrated that CTAB may form adjacent cylindrical micelles by molecular dynamic simulations[14,15]. However, due to challenges in imaging the ligands, such micellar structure has *not* yet been observed experimentally[13,14].

Dynamic motion in a liquid cell

CTAB molecules in water at a concentration of 1 mM (CMC of CTAB) are expected to spontaneously form micelles in a dynamic fashion[54,55]. So far, it has not been possible to directly visualise these dynamics because of a lack of local characterization techniques that enable

investigations under relevant conditions. The liquid environment in a GLC enabled us to overcome these limitations. We indeed observed a micellar structure and even were able to track its movement in the GLC (Fig. 3a-c and Supplementary Movie 2). Intriguingly, we found that the shape of the micelle resembles an ellipsoid before colliding onto an adjacent Au NR. The micelle has an initial size of 12.9 × 8.8 nm, yielding an aspect ratio of ~1.5, in line with previous studies[54,55]. The size of the CTAB micelle is slightly larger than what might be anticipated for a concentration of 1 mM, but local deviations of the overall concentration of the solutions within GLCs are expected due to the stochastic formation of GLCs, resulting in different CTAB concentrations for different liquid cells[56,57]. We could observe this micelle deform upon seemingly attaching to the Au NR.
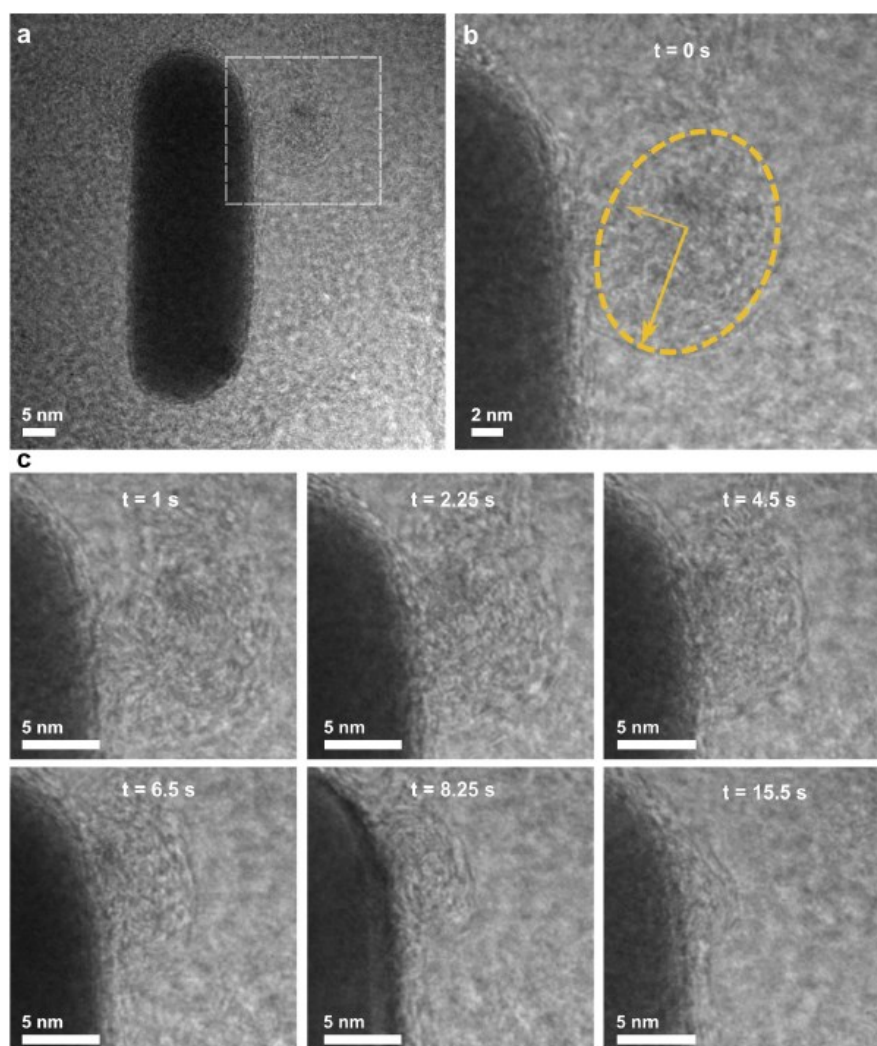
Fig. 3. Dynamic motion of a CTAB micelle in a GLC.a, AC-HRTEM image of a gold NR in a GLC, with a CTAB micelle close to its surface, surrounded by a white dashed square. b, A more detailed AC-HRTEM image of the CTAB micelle shown in a. The dashed orange ellipsoid indicates the approximate long and short axes of the micelle. c, Snapshots of the dynamics of the CTAB micelle from an AC-HRTEM time series (Supplementary Movie 2) showing the attachment of the CTAB micelle to the gold NR.

Our observations challenge the current understanding of the CTAB shell being static and uniform, indicating instead that the shell conformation is more likely to be variable. The presence of micelles at the NR surface is in agreement with molecular dynamics simulations for these systems[14,15,58]. So far, direct experimental confirmation for these simulations was lacking.

Ligand composition and distribution along the surface of the Au NR

To go beyond a solely structural investigation and to further understand the chemical nature of CTAB-capped Au NRs, we performed EDX-STEM imaging in liquid (Fig. 4; Supplementary Figs. 14-17; Supplementary Table 3). Such measurements are challenging and require high quality GLC, without polymer remnants, so that e-beam induced build-up of carbon during the relatively long acquisition times is avoided[41,42]. The TEM holder was first tilted over 15° and a difference in background contrast in the annular dark-field scanning transmission electron microscopy (ADF-STEM) image could be observed near the CTAB-capped Au NRs (Fig. 4a). This contrast difference is due to the presence of liquid and matches the shape of the GLC[52,56]. Next, we measured the K-edge ($K\alpha = 0.525$ keV) X-ray intensity of oxygen inside and outside of the GLC (Fig. 4b; Supplementary Fig. 14a,b), with an intensity ratio of 4.7, which is another confirmation that the GLC has indeed trapped liquid inside[59,60]. More importantly, both Br and

Ag were found to be covering the surface of the Au NRs (Fig. 4c,d; Supplementary Figs. 15a-e and 16a-g). A line profile of the Br intensity indicates a thickness of the CTAB shell of approximately ~ 3 nm (upper panel of Fig. 4e). Moreover, the distribution of Ag overlays well with that of Br (Fig. 4e), indicating that Ag ions are likely to form a complex with bromide at the Au NR surface, as previously reported[34,61,62].
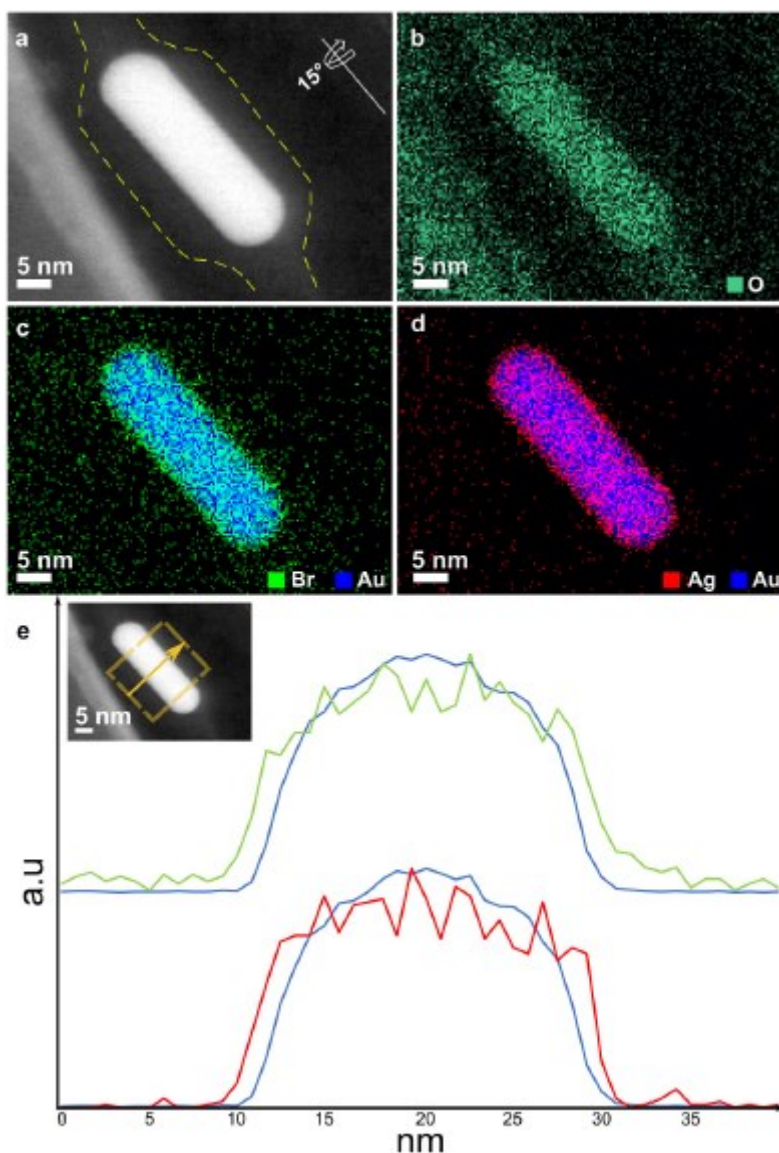

Fig. 4. EDX-STEM analysis of a CTAB-capped gold NR encapsulated in a graphene GLC.

a, ADF-STEM image of an encapsulated gold NR viewed at a 15° tilt angle. The yellow dashed lines denote the shape of the GLC. b–d, EDX chemical mapping of oxygen (b), overlay of gold

and bromine (c), and overlay of silver and gold (d). e, Line profiles across an encapsulated gold NR (inset), showing distributions of bromine (green) and gold (blue) (upper panel) and silver (red) and gold (blue) (lowerpanel). For full spectra and corresponding elemental chemical mappings, see Supplementary Figs. 15 and 16.

Based on the EDX results, the arrangement of the Ag-CTAB complex was further quantified by measuring the ligand density, as explained in Supplementary Fig. 17a-e. These results suggest a lower density of Ag-CTAB at the tips versus the side facets (Supplementary Table 3), in good agreement with earlier theoretical work[34] and with TEM experiments performed under high vacuum conditions[18]. The observed anisotropy in both ligand shell thickness (Fig. 1) and density supports the hypothesis that the Ag-CTAB complex would block specific facets during synthesis and consequently induce symmetry breaking[34].

In conclusion, our study demonstrates the importance of investigating the interface between Au NCs and surface ligands in a liquid environment, rather than in a dried state. Moreover, by exploiting GLCs based on high quality graphene transfer, we found anisotropy in CTAB ligand distribution over the Au NR surface. EDX measurements indicate that Ag ions most likely form a complex with bromine at the Au NR surface. Finally, we directly observed the dynamics of CTAB micelles in a liquid environment, suggesting that the ligand shell is not static and that structural changes may frequently appear. Our results agree with a micelle model for CTAB organisation on Au NRs and, although the measured thickness was found to be in good agreement with earlier work, no clear indications for the formation of a bilayer could be observed. The use of high-quality GLC[63] opens up reliable and direct visualization of ligand distribution around colloidal nanoparticles. Such experiments may be able to explain recent reports, such as the influence of additives such as salycilic acid[64], oleic acid[65], or n-decanol[66],

on the monodispersity of Au nanorods. Also in the currently very active field of chiral nanoparticle growth, visualising the distribution of chiral inducers and understanding how they affect such unusual growth mechanisms will further push the field of anisotropic growth of NPs[4–6]. Our experimental methodology may also enable one to distinguish mixed ligands on the surface of NPs with minute structural damage, complementing other techniques such as scanning tunneling microscopy[13]. Not only being beneficial for the materials science community, we foresee that direct imaging of the so-called protein corona by our approach will promote our understanding in protein-NP interactions that are critical to the design of new diagnosis and therapy strategies for disease treatment[67].

Acknowledgements

Author Contributions Statement

A.P.-T., L.L.-M. and S.B. conceived the project. A.S.-I. prepared the samples and performed

initial characterization. A.P.-T., N.C., D.W., P.N., K.J. and R.D.M. performed all TEM investigations and further analysis. A.P.-T., N.C., D.W., L.L.-M. and S.B. wrote the manuscript with comments from all authors.

Competing Interests Statement

The authors declare no competing interests.

References

1. Sardar, R., Funston, A. M., Mulvaney, P. & Murray, R. W. Gold nanoparticles: past, present, and future. *Langmuir* **25**, 13840–13851 (2009).

2. Liz-Marzán, L. M. *et al.* Celebrating a Nobel prize to the "Discovery of quantum dots, an essential milestone in nanoscience". *ACS Nano* **17**, 19474–19475 (2023).

3. Kovalenko, M. V *et al.* Prospects of nanoscience with nanocrystals. *ACS Nano* **9**, 1012–1057 (2015).

4. Boles, M. A., Ling, D., Hyeon, T. & Talapin, D. V. The surface science of nanocrystals. *Nat. Mater.* **15**, 141–153 (2016).

5. Calvin, J. J., Brewer, A. S. & Alivisatos, A. P. The role of organic ligand shell structures in colloidal nanocrystal synthesis. *Nat. Synth.* **1**, 127–137 (2022).

6. Gómez-Graña, S. *et al.* Surfactant (bi)layers on gold nanorods. *Langmuir* **28**, 1453–1459 (2012).

7. Hore, M. J. A. *et al.* Probing the structure, composition, and spatial distribution of ligands on gold nanorods. *Nano Lett.* **15**, 5730–5738 (2015).

8. Seibt, S., Zhang, H., Mudie, S., Förster, S. & Mulvaney, P. Growth of gold nanorods: a SAXS study. *J. Phys. Chem. C* **125**, 19947–19960 (2021).

9. García, I. *et al.* Residual CTAB ligands as mass spectrometry labels to monitor cellular uptake of Au nanorods. *J. Phys. Chem. Lett.* **6**, 2003–2008 (2015).

10. Nikoobakht, B. & El-Sayed, M. A. Evidence for bilayer assembly of cationic surfactants on the surface of gold nanorods. *Langmuir* **17**, 6368–6374 (2001).

11. Grzelczak, M. *et al.* Influence of iodide ions on the growth of gold nanorods: tuning tip curvature and surface plasmon resonance. *Adv. Funct. Mater.* **18**, 3780–3786 (2008).

12. Mosquera, J., Wang, D., Bals, S. & Liz-Marzán, L. M. Surfactant layers on gold nanorods. *Acc. Chem. Res.* **56**, 1204–1212 (2023).

13. Ong, Q., Luo, Z. & Stellacci, F. Characterization of ligand shell for mixed-ligand coated gold nanoparticles. *Acc. Chem. Res.* **50**, 1911–1919 (2017).

14. Meena, S. K. & Sulpizi, M. Understanding the microscopic origin of gold nanoparticle anisotropic growth from molecular dynamics simulations. *Langmuir* **29**, 14954–14961 (2013).

15. Meena, S. K. & Sulpizi, M. From gold nanoseeds to nanorods: The microscopic origin of the anisotropic growth. *Angew. Chem. Int.* **128**, 12139–12143 (2016).

16. Choi, M.-H. *et al.* Characterization of ligand adsorption at individual gold nanocubes. *Langmuir* **37**, 7701–7711 (2021).

17. Kim, J.-Y. *et al.* Dipole-like electrostatic asymmetry of gold nanorods. *Sci. Adv.* **4**, e1700682 (2018).

18. Janicek, B. E. *et al.* Quantitative imaging of organic ligand density on anisotropic inorganic nanocrystals. *Nano Lett.* **19**, 6308–6314 (2019).

19. Lee, Z. *et al.* Direct Imaging of soft−hard interfaces enabled by graphene. *Nano Lett.* **9**, 3365 (2009).

20. Pantelic, R. S., Meyer, J. C., Kaiser, U. & Stahlberg, H. The application of graphene as a sample support in transmission electron microscopy. *Solid State Commun.* **152**, 1375–1382 (2012).

21. Zhu, Y. *et al.* Graphene and graphene oxide: Synthesis, properties, and applications. *Adv. Mater.* **22**, 3906–3924 (2010).

22. Algara-Siller, G., Kurasch, S., Sedighi, M., Lehtinen, O. & Kaiser, U. The pristine atomic structure of MoS_2 monolayer protected from electron radiation damage by graphene. *Appl. Phys. Lett.* **103**, 203107 (2013).

23. Zan, R. *et al.* Control of Radiation Damage in MoS_2 by Graphene Encapsulation. *ACS Nano* **7**, 10167–10174 (2013).

24. Hudry, D. *et al.* Interface pattern engineering in core-shell upconverting nanocrystals: shedding light on critical parameters and consequences for the photoluminescence properties. *Small* **17**, 2104441 (2021).

25. Panthani, M. G. *et al.* Graphene-supported STEM imaging of Si and their capping ligands. *J. Phys. Chem. C* **116**, 22463–22468 (2012).

26. Nair, R. R., Blake, P., Blake, J. R., Zan, R. & Anissimova, S. Graphene as a transparent conductive support for studying biological molecules by transmission electron microscopy. *Appl. Phys. Lett.* **153102**, 1–4 (2011).

27. Meyer, J. C., Girit, C. O., Crommie, M. F. & Zettl, A. Imaging and dynamics of light atoms and molecules on graphene. *Nature* **454**, 1–9 (2008).

28. Han, Y. *et al.* High-yield monolayer graphene grids for near-atomic resolution cryoelectron microscopy. *Proc. Natl. Acad. Sci. U.S.A.* **117**, 1009–1014 (2020).

29. Rogolino, A. *et al.* Metal–polymer heterojunction in colloidal-phase plasmonic catalysis. *J. Phys. Chem. Lett.* 2264–2272 (2022).

30. Park, J. *et al.* Graphene liquid cell electron microscopy: Progress, applications, and perspectives. *ACS Nano* **15**, 288–308 (2021).

31. Textor, M. & de Jonge, N. Strategies for preparing graphene liquid cells for transmission electron microscopy. *Nano Lett.* **18**, 3313–3321 (2018).

32. Murphy, C. J. *et al.* The many faces of gold nanorods. *J. Phys. Chem. Lett.* **1**, 2867–2875 (2010).

33. Moreau, L. M. *et al.* The role of trace Ag in the synthesis of Au nanorods. *Nanoscale* **11**, 11744–11754 (2019).

34. Almora-Barrios, N., Novell-Leruth, G., Whiting, P., Liz-Marzán, L. M. & López, N. Theoretical description of the role of halides, silver, and surfactants on the structure of gold nanorods. *Nano Lett.* **14**, 871–875 (2014).

35.   Ye, X., Zheng, C., Chen, J., Gao, Y. & Murray, C. B. Using binary surfactant mixtures to simultaneously improve the dimensional tunability and monodispersity in the seeded growth of gold nanorods. *Nano Lett.* **13**, 765–771 (2013).

36.   Goris, B. *et al.* Atomic-scale determination of surface facets in gold nanorods. *Nat. Mater.* **11**, 930–935 (2012).

37.   Claes, N. *et al.* Characterization of silver-polymer core-shell nanoparticles using electron microscopy. *Nanoscale* **10**, 9186–9191 (2018).

38.   Kang, J., Shin, D., Bae, S. & Hong, B. H. Graphene transfer: key for applications. *Nanoscale* **4**, 5527–5537 (2012).

39.   Zhang, T. *et al.* Clean transfer of 2D transition metal dichalcogenides using cellulose acetate for atomic resolution characterizations. *ACS Appl. Nano. Mater.* **2**, 5320–5328 (2019).

40.   De Meyer, R., Albrecht, W. & Bals, S. Effectiveness of reducing the influence of CTAB at the surface of metal nanoparticles during in situ heating studies by TEM. *Micron* **144**, 103036 (2021).

41.   Li, C. *et al.* A simple method to clean ligand contamination on TEM grids. *Ultramicroscopy* **221**, 113195 (2021).

42.   Algara-Siller, G., Lehtinen, O., Turchanin, A. & Kaiser, U. Dry-cleaning of graphene. *Appl. Phys. Lett.* **104**, 153115 (2014).

43.   Urban, K. W. *et al.* Negative spherical aberration ultrahigh-resolution imaging in corrected transmission electron microscopy. *Philos. Trans. R. Soc. A* **367**, 3735–3753 (2009)

44.   Yu, Y., Cui, F., Sun, J. & Yang, P. Atomic structure of ultrathin gold nanowires. *Nano Lett*. **16**, 3078–3084 (2016).

45.   Silva, J., Dias, R., Da Hora, G., Soares, T. & Meneghetti, M. Molecular dynamics simulations of cetyltrimethylammonium bromide (CTAB) micelles and their interactions with a gold surface in aqueous solution. *J. Braz. Chem. Soc.* **29**, (2017).

46.   Yuk, J. M. *et al.* High-resolution EM of colloidal nanocrystal growth using graphene liquid cells. *Science* **336**, 61–64 (2012).

47.   Dachraoui, W., Henninen, T. R., Keller, D. & Erni, R. Multi-step atomic mechanism of platinum nanocrystals nucleation and growth revealed by in-situ liquid cell STEM. *Sci. Rep.* **11**, 23965 (2021).

48.   Wang, C., Shokuhfar, T. & Klie, R. F. Precise in situ modulation of local liquid chemistry via electron irradiation in nanoreactors based on graphene liquid cells. *Adv. Mater.* **28**, 7716–7722 (2016).

49.   Hermannsdörfer, J., Tinnemann, V., Peckys, D. B. & de Jonge, N. The effect of electron beam irradiation in environmental scanning transmission electron microscopy of whole cells in liquid. *Microsc. Microanal.* **22**, 656–665 (2016).

50.   Cho, H. *et al.* The use of graphene and its derivatives for liquid-phase transmission electron microscopy of radiation-sensitive specimens. *Nano Lett.* **17**, 414–420 (2017).

51. Keskin, S. & de Jonge, N. Reduced radiation damage in transmission electron microscopy of proteins in graphene liquid cells. *Nano Lett.* **18**, 7435–7440 (2018).

52. Khestanova, E., Guinea, F., Fumagalli, L., Geim, A. K. & Grigorieva, I. V. Universal shape and pressure inside bubbles appearing in van der Waals heterostructures. *Nat. Commun.* **7**, 12587 (2016).

53. Ghodsi, S. M. *et al.* Assessment of pressure and density of confined water in graphene liquid cells. *Adv. Mater. Interfaces.* **7**, 1901727 (2020).

54. Bergström, L. M. & Grillo, I. Correlation between the geometrical shape and growth behaviour of surfactant micelles investigated with small-angle neutron scattering. *Soft Matter* **10**, 9362–9372 (2014).

55. Skoglund, S. *et al.* A novel explanation for the enhanced colloidal stability of silver nanoparticles in the presence of an oppositely charged surfactant. *Phys. Chem. Chem. Phys.* **19**, 28037–28043 (2017).

56. Yuk, J. M. *et al.* Graphene veils and sandwiches. *Nano Lett.* **11**, 3290–3294 (2011).

57. Crook, M. F. *et al.* EELS studies of cerium electrolyte reveal substantial solute concentration effects in graphene liquid cells. *J. Am. Chem. Soc.* **145**, 6648–6657 (2023).

58. Meena, S. K. *et al.* The role of halide ions in the anisotropic growth of gold nanoparticles: a microscopic, atomistic perspective. *Phys. Chem. Chem. Phys.* **18**, 13246–13254 (2016).

59. Kelly, D. J. *et al.* Nanometer resolution elemental mapping in graphene-based TEM liquid cells. *Nano Lett.* **18**, 1168–1174 (2018).

60. Lewis, E. A. *et al.* Real-time imaging and local elemental analysis of nanostructures in liquids. *Chem. Commun.* **50**, 10019–10022 (2014).

61. González-Rubio, G., Scarabelli, L., Guerrero-Martínez, A. & Liz-Marzán, L. M. Surfactant-assisted symmetry breaking in colloidal gold nanocrystal growth. *ChemNanoMat* **6**, 698–707 (2020).

62. Hubert, F., Testard, F. & Spalla, O. Cetyltrimethylammonium bromide silver bromide complex as the capping agent of gold nanorods. *Langmuir* **24**, 9219–9222 (2008).

63. A. Pedrazo Tardajos, S. Bals, GRAPHENE LAYER TRANSFER METHOD (2020), (available at https://patents.google.com/patent/EP4011828A1/en?oq=EP4011828A1).

64. Scarabelli, L., Grzelczak, M. & Liz-Marzán, L. M. Tuning gold nanorod synthesis through prereduction with salicylic acid. *Chem. Mater.* **25**, 4232–4238 (2013).

65. Ye, X., Zheng, C., Chen, J., Gao, Y. & Murray, C. B. Using binary surfactant mixtures to simultaneously improve the dimensional tunability and monodispersity in the seeded growth of gold nanorods. *Nano Lett.* **13**, 765–771 (2013)

66. González-Rubio, G. *et al.* Disconnecting symmetry breaking from seeded growth for the reproducible synthesis of high quality gold nanorods. *ACS Nano* **13**, 4424–4435 (2019).

67. He, Z., Qu, S. & Shang, L. Perspectives on protein–nanoparticle interactions at the *in vivo* level. *Langmuir* (2024).

Methods

Graphene transfer

The polymer solution used to create the protective coating was prepared by the combination CAB (Merck) and ethyl acetate (see Supplementary Methods for details), mixed using a magnetic stirrer. This solution was kept at room temperature. A monolayer of graphene on copper foil (Graphenea, 10 mm × 10 mm) produced by CVD was covered by an ultra-thin layer (See Supplementary Methods for more details) of the resulting polymer using a dip-coating method (Supplementary Fig. 2a). The backside of the copper foil was carefully washed several times using acetone. Afterwards, the copper foil was placed on the surface of an etching solvent, an aqueous solution prepared using 0.7 g of ammonium persulfate ($(NH_4)_2S_2O_8$) and 100 mL of ultrapure water, for one-two hours approximately (Supplementary Fig. 2b). As an extra step, the etching solution was diluted with ultrapure water until the approximate value of the latest (pH ≈ 5.85) (Supplementary Fig. 2c). Once the process was completed, holey carbon coated Au TEM grids (Quantifoil, 200 mesh, holes with 2 µm in diameter) were introduced in the water solution on a filter paper at the bottom of the petri dish (Supplementary Fig. 2d). Water was slowly removed, ensuring that the floating graphene and polymer layer were deposited on the grids (Supplementary Fig. 2e). Finally, the grids were dried at 35 °C for 30 min (Supplementary Fig. 2f). Prior to use, the grids were heat treated by heating the sample in activated carbon to remove the CAB remnants effectively (Supplementary Fig. 2g)[1,2]. The graphene grid was placed in between activated carbon and heated up to 300 °C (with a ramp of 5 °C/min) for 15 hours.

Graphene liquid cell (GLC)

The process to create a GLC starts with the etching of copper foil (Supplementary Fig. 6a), followed by dilution of the etching solution (Supplementary Fig. 6b). After that, the graphene

cell might be sealed from the bottom (Supplementary Fig. 6c). Encapsulation from the top was performed by first drop-casting the dispersion containing Au NRs with CTAB 1 mM on an ultra-clean graphene TEM grid and, before the solution evaporated, stamping the grid on the graphene flake (Supplementary Fig. 6c). On the other hand, after neutralization of the solvent, an ultra-clean graphene TEM grid was deposited under the floating graphene flake and the solution was exchanged for an aqueous solution of CTAB with a concentration of 1 mM. Then, the solution was removed while drop-casting 7 µL of the Au NRs dispersion with CTAB in solution. Finally, all the liquid was removed and the graphene flake floating on the liquid fell onto the flake at the bottom, forming sealed cells. In this manner, the flatness and homogeneity of the encapsulation can be ensured[3].

Transmission electron microscopy (TEM)

TEM images at low magnification were obtained with a JEOL JEM-1400PLUS transmission electron microscope operating at an acceleration voltage of 120 kV, using carbon-coated 400 square mesh copper grids.

Aberration-corrected high-resolution TEM (AC-HRTEM) images were acquired using an aberration-corrected Thermo Fisher Scientific Titan operated at 80 kV using a monochromator and a negative spherical aberration (Cs = -5 µm). Au NRs capped by CTAB or PEG-SH were visualised using a Gatan US1000XP camera with an electron dose of 300 e⁻ per image.

ADF-STEM imaging, EDX-STEM were performed using a Thermo Fisher Scientific Osiris electron microscope operated at 200 kV at a camera length of 115 mm. The EDX-STEM datasets were acquired with a 233 pA beam current and a total time acquisition of approximately 12 min.

A detailed overview of the electron dose for different images in the manuscript can be found in Supplementary Table 4.

Electron energy loss spectroscopy (EELS)

EELS experiments to determine the GLC thickness were performed using an aberration-corrected Thermo Fisher Scientific Titan microscope operated at 80 kV. High angle annular dark field STEM images were acquired using a 50 pA beam current and a camera length of 115 mm. An energy resolution of 0.16-0.20 eV (full width half maximum of zero loss peak (ZLP)) was achieved by exciting a monochromator (Wien filter) to 0.7. The thickness variation across the GLC was calculated using the log-ratio (relative) routine. The thickness t is computed as a multiple of the inelastic mean free path λ using the following equation: $t = \lambda \cdot \ln\left(\frac{I_t}{I_0}\right)$, where I_0 is the integrated area under the ZLP, I_t is the total integrated area (counts) under the whole spectrum. The value of λ for water using 200 keV is 106 nm. For 80 keV the values will be about a factor of 1.5 lower, i.e. ~70 nm[4].

Data Availability

Additional and raw data related to this paper is included in this published article and its Supplementary Information.

Methods-only references

1. Zhang, T. *et al.* Clean transfer of 2D transition metal dichalcogenides using cellulose acetate for atomic resolution characterizations. *ACS Appl. Nano. Mater.* **2**, 5320–5328 (2019).

2. Algara-Siller, G., Lehtinen, O., Turchanin, A., & Kaiser, U. Dry-cleaning of graphene. *Appl. Phys. Lett.* **104**, 153115 (2014).

3. Boscá, A., Pedrós, J., Martínez, J., Palacios, T. & Calle, F. Automatic graphene transfer system for improved material quality and efficiency. *Sci. Rep.* **6**, 21676 (2016).

4. Holtz, M. E., Yu, Y., Gao, J., Abruña, H. D., & Muller, D. A. In situ electron energy-loss spectroscopy in liquids. *Microsc. Microanal.* **19**, 1027-103 (2013).